Journal of Physics and Chemistry of Solids 212 (2026) 113517

Contents lists available at ScienceDirect

Journal of Physics and Chemistry of Solids

journal homepage: www.elsevier.com/locate/jpcs

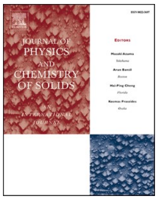

Synthesis of a magnetically heatable ceria–supported ruthenium catalyst via deposition of nanocrystalline ceria on silica-coated magnetic iron–oxide nanoparticles

Nina Križaj Kosi[a,b,*], Jakov-Stjepan Pavelić[c], Miha Grilc[c], Sašo Gyergyek[a], Darko Makovec[a,b,**]

[a] Department for Materials Synthesis, Jožef Stefan Institute, Slovenia
[b] Jožef Stefan International Postgraduate School, Slovenia
[c] Department for Catalysis and Chemical Reaction Engineering, National Institute of Chemistry, Slovenia

ARTICLE INFO

Keywords:
Catalyst synthesis
Ceria
Magnetic nanoparticles
Catalysis by magnetic heating
Biomass valorisation
Transmission electron microscopy

ABSTRACT

We report the synthesis of a ceria-based catalyst support containing embedded magnetic iron–oxide nanoparticles (IONPs) that enable heating under a high-frequency alternating magnetic field. The ≈11 nm IONPs, synthesized by co-precipitation of Fe^{2+}/Fe^{3+} ions at room temperature, were coarsened to ≈18 nm through subsequent hydrothermal treatment at 120 °C and then coated with a ≈2 nm silica layer. The catalyst support was prepared by depositing nanocrystalline ceria (CeO_2) onto the IONPs via controlled precipitation of Ce^{3+} ions in the presence of hexamethylenetetramine (HMTA) in aqueous suspension. When deposited directly on the iron oxide, ceria formed small agglomerates of ≈10 nm octahedral nanocrystallites, whereas deposition on silica-coated IONPs produced a homogeneous 3–6 nm-thick shell composed of ≈3 nm globular crystallites. Special attention was given to elucidating the mechanism of shell formation. The magnetic catalyst was obtained by precipitating Ru nanoparticles (1–2 nm) onto the ceria support. Morpho-structural characterization was performed by XRD, TEM, and aberration-corrected STEM. Static and dynamic magnetization measurements at room temperature were used to assess the magnetic and heating performance. At low field amplitudes (<15 mT), catalysts prepared with IONPs of both sizes exhibited similar specific absorption rates, whereas at higher amplitudes the larger IONPs demonstrated superior heating efficiency. The catalytic performance was demonstrated in the magnetically heated hydrogenation of the bio-based compound 5-(hydroxymethyl)furfural to 2,5-bis(hydroxymethyl)furan, showing high activity, 100 % selectivity, and excellent stability upon recycling.

1. Introduction

The electrification of the chemical industry is one of the most important challenges in the transition to a carbon-neutral society. A key advantage of electrified processes is the possibility of using surplus renewable electricity for the production of fuels (e.g., H_2, NH_3, and biofuels) and bio-based chemicals. The vast majority of the chemical processes involved rely on heterogeneous catalysis [1–3].

Catalysis by magnetic heating (also referred to as induction heating) is an emerging technology that enables efficient use of electricity to supply heat for thermocatalytic processes. This approach is based on heating magnetic nanoparticles (MNPs, a list of all abbreviation and symbols is given in the Supplementary material (SI)) embedded into the catalyst support within a high-frequency (100–600 kHz) alternating magnetic field (AMF) [4–7]. The AMF is typically generated by a coil into which the reactor vessel is inserted, and the MNPs act as localized heat sources that transfer heat to the catalyst. Because MNPs dissipate heat locally, the catalyst is selectively heated from the interior, resulting in surface temperatures significantly higher than those of the bulk reaction medium [8–10]. For example, in the hydrogenation of levulinic acid to γ-valerolactone via magnetic heating of Ru nanocatalyst, the catalyst surface reached 137 °C while the bulk reaction medium remained at 85 °C [10].

This localized heating can lead to substantial improvements in

---

* Corresponding author. Department for Materials Synthesis, Jožef Stefan Institute, Slovenia.
** Corresponding author. Department for Materials Synthesis, Jožef Stefan Institute, Slovenia.
E-mail addresses: nina.krizaj@ijs.si (N. Križaj Kosi), darko.makovec@ijs.si (D. Makovec).

https://doi.org/10.1016/j.jpcs.2026.113517
Received 23 October 2025; Received in revised form 5 January 2026; Accepted 5 January 2026

selectivity and yields under mild conditions [10], providing a strong basis for improving process energy efficiency. Compared to conventional heating methods (e.g., gas burners and resistive heating), magnetic heating offers much higher heating and cooling rates, which enables the design of reactors with optimized hydrodynamics. As a result, many catalytic reactions can be shifted from heat-transfer limitations to kinetic control [4]. Moreover, with its improved responsiveness and flexibility, magnetic heating is particularly well suited for decentralized, adaptable, containerized, and fast-reacting electrified units capable of responding to sudden fluctuations in the availability of renewable electricity from sources such as solar panels and wind turbines.

Magnetic catalysis has already been successfully applied in a range of applications, including the synthesis of fine chemicals [4–21], fuels [22–31], and the decomposition of water pollutants [32]. Depending on the requirements of the catalytic reaction, different magnetic catalysts have been synthesized. Typically, a magnetic catalyst consists of small catalytic nanoparticles deposited on a high–surface-area support in which MNPs are incorporated. The magnetic material of the MNPs is chosen according to its heating ability in an AMF and its chemical stability.

MNPs generate heat primarily through hysteresis losses. The amount of heat produced depends on the MNP content and on their properties, which define the area of the dynamic magnetic hysteresis loop at the applied field frequency [4–7]. For high-temperature applications under reducing conditions—such as catalytic processes in hydrogen-containing atmospheres—metallic MNPs (e.g., Fe^0, Ni^0, Co^0), their alloys [12,13,18,21,23–25,29–31,33], or iron–carbide MNPs [9,20,22,26] are preferred. For use under oxidizing or mildly reducing conditions, magnetic iron–oxide nanoparticles (magnetite or maghemite) are preferred because of their low cost and straightforward synthesis [10,11,15–17,19].

MNPs, which provide localized magnetic heating of the catalyst, are typically incorporated into a catalyst support with a large surface area. The support stabilizes both the magnetic and catalytic nanoparticles during long-term catalytic processes at elevated temperatures. At the same time, it can significantly improve the efficiency of catalyst through interactions with the catalytic nanoparticles and the reactants/products. Carbon [10,18], alumina [19], silica–alumina [26], and $MgAl_2O_4$ [23] have already been used as nanostructured supporting materials for magnetic catalysts.

Nanostructured ceria (CeO_2) is a preferred support material for many catalytic reactions, including reforming, CO oxidation, methane partial oxidation, volatile organic compound oxidation, soot oxidation, the water–gas shift reaction, and the deoxygenation of fatty acids. With its high oxygen storage capacity and unique redox properties—dominated by rapid switching of the oxidation state between Ce^{4+} and Ce^{3+}—ceria can strongly enhance the oxidation activity of catalysts, largely due to the low activation barrier for creating lattice oxygen vacancies. Moreover, Lewis acid sites on the reducible ceria surfaces, along with spillover effects, can improve deoxygenation reactions [34–36].

A simple strategy for synthesizing magnetic ceria supports involves depositing a nanocrystalline ceria shell onto pre-synthesized MNPs. The shell can be formed by controlled precipitation of Ce^{3+} ions. During the controlled precipitation, the supersaturation of the precipitating species must be kept low and closely controlled to ensure exclusively heterogeneous nucleation on the core nanoparticles dispersed in the reaction solution [37]. Nanocrystalline ceria coatings have already been deposited onto various core particles by precipitating Ce^{3+} ions in the presence of hexamethylenetetramine (HMTA) in aqueous suspension [38–42]. The resulting shells were relatively smooth and composed of tightly packed ceria nanocrystallites approximately 5 nm in size.

In this study, we report a method for synthesis of magnetic ceria catalyst supports. The magnetic support was prepared by depositing ceria onto magnetic iron–oxide nanoparticles. Special attention was given to elucidating the chemical mechanisms that enable the deposition of nanocrystalline ceria coatings. After depositing catalytic Ru nanoparticles onto the magnetic ceria supports their heating ability and catalytic efficiency were demonstrated in the magnetically heated catalytic hydrogenation of 5-(hydroxymethyl)furfural (HMF).

2. Experimental

2.1. Synthesis of magnetic nanoparticles

Magnetic iron–oxide nanoparticles (C–IONPs) were synthesized by co-precipitation of Fe^{2+} and Fe^{3+} ions with ammonia at room temperature, as reported before [43]. To increase the size of co-precipitated magnetic nanoparticles, the C–IONPs were hydrothermally treated for 6 h at 120 °C after co-precipitation. Hydrothermally-treated nanoparticles were labelled as HT–IONPs. Both types of magnetic nanoparticles, C–IONPs and HT–IONPs, were subsequently coated with a thin layer of silica using hydrolysis and polycondensation of tetraethyl orthosilicate (TEOS) in their colloidally-stable aqueous suspensions stabilized by citric acid, as described elsewhere [44]. The silica–coated magnetic nanoparticles were labelled as C–IONP–SIL and HT–IONP–SIL. Details of the synthesis procedures are given in the SI.

2.2. Deposition of ceria shell onto the magnetic nanoparticles

A ceria shell was deposited onto the magnetic nanoparticles using a modified method based on controlled precipitation of Ce^{3+} ions in the presence of hexamethylenetetramine (HMTA), which was first reported by Cui et al. [39]. In standard procedure, magnetic nanoparticles (naked nanoparticles C-IONP/HT-IONP, or silica-coated nanoparticles C-IONP-SIL/HT-IONP-SIL) were dispersed in 80 mL of an ethanol/water mixture (6 mg/mL; ethanol/water volume ratio = 1). An aqueous solution of $Ce(NO_3)_3$ (3.42 mmol; Ce^{3+}/IONP–SIL mass ratio = 1) was first added to the suspension, followed by the addition of an aqueous solution of HMTA (6.84 mmol; HMTA/Ce^{3+} molar ratio = 2). The pH of the suspension was then adjusted to 8.0 using aqueous ammonia solution. The suspension was heated to 65 °C at a rate of 0.3 °C/min, maintained under reflux for 2 h, and then rapidly cooled to room temperature. The resulting nanocomposite was collected and washed three times with water by sedimentation with centrifugation. To avoid the strong agglomeration usually observed after conventional drying of nanostructured materials at elevated temperatures, the wet product was frozen in liquid nitrogen and then freeze-dried over the course of two days.

To evaluate the influence of different experimental parameters (such as Ce^{3+}/IONP–SIL mass ratio, HMTA/Ce^{3+} molar ratio, suspension pH, final temperature, etc.) on the properties of the synthesized nanocomposite, individual parameters from the standard procedure were systematically varied while all other parameters were kept constant. The same procedure was also used for the synthesis of ceria nanoparticles in the absence of IONPs in the reaction mixture.

2.3. Deposition of catalytic Ru nanoparticles onto the magnetic ceria support

For magnetic and catalytic characterization, two magnetic catalysts were prepared. The two catalysts differed in the type of incorporated magnetic nanoparticles: catalyst C–Ru contained smaller co-precipitated nanoparticles (C–IONP–SIL), whereas catalyst HT–Ru contained larger hydrothermally-treated nanoparticles (HT–IONP–SIL). First, magnetic ceria supports were synthesized by depositing a ceria shell onto silica-coated magnetic iron-oxide nanoparticles (C–IONP–SIL or HT–IONP–SIL) using the standard procedure. Subsequently, Ru nanoparticles were deposited onto the ceria support by precipitation of the Ru^{3+} ions with NaOH. Aqueous solution of $RuCl_3$ was added to 50 mL of suspension containing the nanoparticles of magnetic ceria support (10 mg/mL) suspended in diluted HNO_3 solution at pH 3.5. The suspension was stirred for 30 min while maintaining the pH at 3.5. Then, the pH of the suspension was increased to 9.8 using aqueous NaOH solution. The resulting nanocomposite was collected and washed three times with water by sedimentation with centrifugation. The wet product was frozen in liquid nitrogen and subsequently freeze-dried over the course of two days. The final catalytic Ru nanoparticles were obtained by atmospheric reduction of the nanocomposite at 250 °C for 1 h under a flow of H_2.

2.4. *Characterisation*

Morpho-structural characterization of the samples was carried out using a transmission electron microscopy (TEM, JEOL 2100) and an aberration-probe-corrected scanning-transmission electron microscopy (STEM, JEOL ARM 200CF) combined with energy-dispersive X-ray spectroscopy (EDXS). X-ray powder diffraction (XRD) patterns were recorded using a PANalytical X'Pert PRO diffractometer. The specific surface area of the catalysts was determined from nitrogen adsorption/desorption isotherms measured with a nitrogen sorption analyser (BET, Quantachrome Nova 2000e). The Ru and Fe content in the catalysts was determined using an energy-dispersive X-ray fluorescence (XRF) spectrometer [45].

Magnetic properties were measured with a vibrating-sample magnetometer (VSM, Lake Shore 7307) at room temperature. Saturation magnetizations (M_S) were obtained by fitting the positive branch of the magnetization curve with $M = M_s(a/\mu_0 H - b/(\mu_0 H)^2) + \chi \mu_0 H$ in the field range $0.2\ T < \mu_0 H < 1\ T$. Room-temperature dynamic hysteresis loops were measured with an Advance AC Hyster™ magnetometer (Nanotech Solutions) at 112 kHz. For these measurements, the powdered samples were compacted to a volume of 12 μL in an NMR tube (76 mm long, 3 mm outer diameter, 0.27 mm wall thickness) and compressed with a ball made of Teflon tape. The tube was then inserted into the instrument, which measures dynamic hysteresis loops; the specific absorption rate (SAR) was calculated from the loop area A according to SAR = f·A, where f is the frequency. Mass magnetizations reported in $A\cdot m^2/kg$ refer to magnetization per kilogram of total sample, whereas values given in $A\cdot m^2/kg_{IONP}$ refer to magnetization per kilogram of iron-oxide nanoparticles (IONPs). The IONP masses were calculated as Fe_2O_3 equivalents from the Fe content determined by XRF. Details of the characterization methods are provided in the SI.

2.5. *Testing of the magnetic catalysts in catalytic reactions*

Photographs of the magnetic reactor and a schematic representation of the experimental setup are shown in Fig. 1. The 1.50 g of the magnetic catalyst was suspended in 40 mL of tetrahydrofuran (THF) containing 5.0 g of dissolved 5-(hydroxymethyl)furfural (HMF) in a round-bottom glass pressure vessel. The vessel was sealed and flushed five times with Ar, followed by five flushes with H_2, and then pressurized with H_2 to 1 MPa. Throughout the hydrotreatment, the total pressure was maintained at 1 MPa using H_2 supplied from a cylinder. A Teflon-made Rushton turbine, driven by an overhead stirrer, was used to solubilize H_2 and disperse the catalyst. The reactor head was equipped with a gas inlet/outlet and a sampling line that enabled cooling of the sample below room temperature before releasing it into the collection vessel (to prevent THF evaporation). An N-type thermocouple (showing negligible heating in the AMF) was inserted into the reaction vessel to continuously monitor the temperature. The reactor vessel was insulated with 2 mm-thick quartz paper and placed inside a copper-tube induction coil (5.5 × 5.5 mm insulated square tubing, wound into a 9-turn coil with a height of 70 mm and an inner diameter of 60 mm) connected to an Ultraflex UPT-n2 generator. Liquid samples collected at specified reaction times (after immediate catalyst removal by magnetic separation) were diluted

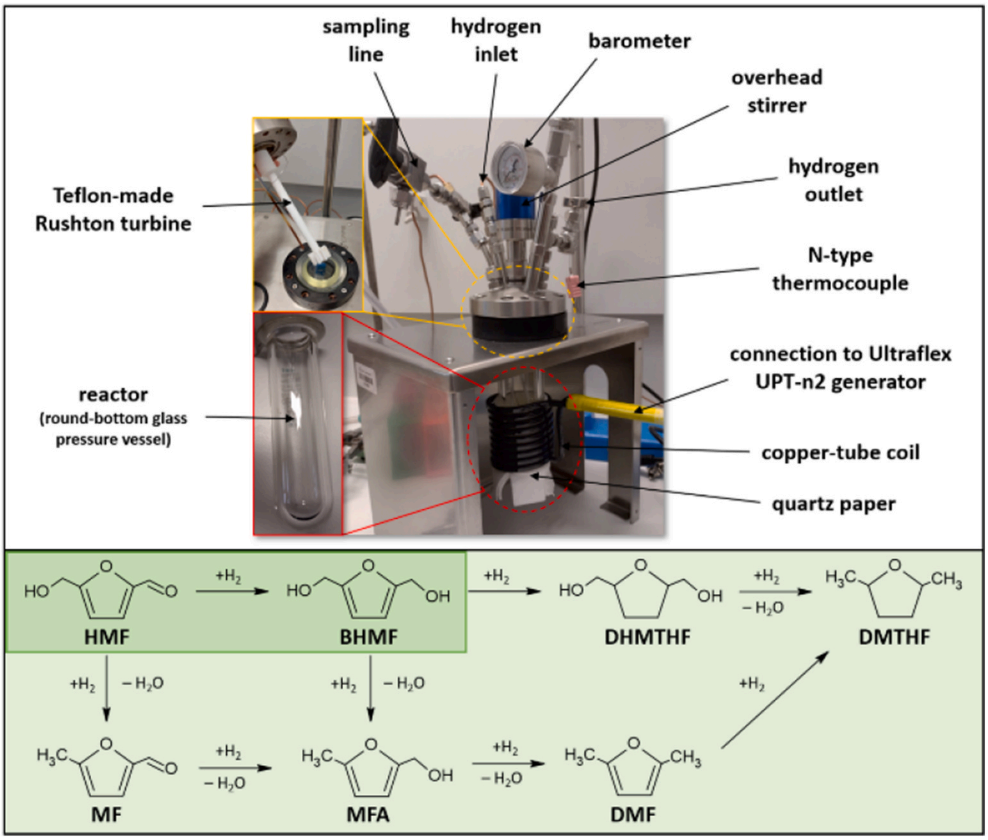

Fig. 1. A schematic representation of the experimental setup for testing of the magnetic catalysts in catalytic hydrogenation of HMF (HMF: 5-(hydroxymethyl) furfural, BHMF: 2,5-bis(hydroxymethyl)furan, DHMTHF: 2,5-di(hydroxymethyl)tetrahydrofuran, DMTHF: 2,5-dimethyltetrahydrofuran, MF: 5-methylfurfural, MFA: (5-methyl-2-furyl)methanol, DMF: 2,5-dimethylfuran).

with acetone and analysed by GC-QMS (Ultra 2010, Shimadzu, Japan). After each run, the recovered catalyst was washed five times with pure THF and reused in four subsequent reaction cycles under identical conditions and catalyst loadings.

3. Results and discussion

3.1. *Magnetic iron-oxide core nanoparticles*

Ceria was deposited on naked magnetic core nanoparticles (C-IONP and HT-IONP) and on silica-coated magnetic nanoparticles (C-IONP-SIL and HT-IONP-SIL). The C–IONPs, precipitated at room temperature, had a globular shape with a size of 11.2 ± 4.1 nm, measured from TEM images (d_{TEM}, expressed as an equivalent diameter). The XRD pattern of the C–IONPs showed broadened diffraction peaks corresponding to the spinel structure of iron oxide (maghemite or magnetite). Their size (d_{XRD}), estimated from XRD peak broadening, was 15 nm. VSM measurements showed a slim hysteresis loop with low remanence ($M_R = 3.0$ A m^2/kg), coercivity ($\mu_0 Hc = 2.7$ mT), and a saturation magnetization (M_S) of 65.7 A m^2/kg (Table 1). Coating with silica produced a relatively homogeneous silica layer. TEM analysis revealed that individual magnetic nanoparticles were typically covered with a ≈2 nm-thick silica layer; however, in some cases, small agglomerates of 2–5 magnetic cores were coated together. After coating with nonmagnetic silica, the M_S of C–IONP–SIL decreased to 33.8 A m^2/kg due to dilution of magnetic nanoparticles with nonmagnetic silica (Table 1).

To increase nanoparticle size for improved magnetic heating, the C–IONPs obtained by co-precipitation at room temperature were subjected to hydrothermal treatment for 6 h at 120 °C. After hydrothermal treatment, the HT–IONPs retained the spinel structure but grew to $d_{TEM} = 18.4 \pm 4.2$ nm and $d_{XRD} = 20$ nm. Despite the increased size, they retained a slim hysteresis loop ($M_R = 5.5$ A m^2/kg; $\mu_0 Hc = 7.2$ mT) with high initial susceptibility and $M_S = 70.8$ A m^2/kg (Table 1). After silica coating, the M_S of HT–IONP–SIL decreased to 44.2 A m^2/kg. TEM images, XRD patterns, and magnetic hysteresis loops are provided in the SI (Fig. SI1–SI4).

3.2. *Deposition of ceria shell*

Ceria was deposited onto the magnetic core nanoparticles by controlled precipitation of Ce^{3+} ions in the presence of HMTA in aqueous suspension. To develop and evaluate the deposition method, co-precipitated magnetic iron–oxide nanoparticles, both before (C–IONP) and after coating with a thin layer of silica (C-IONP-SIL), were used as the cores.

When Ce^{3+} ions were precipitated in the presence of HMTA without any core nanoparticles in the reaction mixture, ceria nanoparticles with a relatively uniform size of ≈5 nm were formed (Fig. 2). Electron diffraction revealed a pattern (inset of Fig. 2(b)) composed of broad diffraction rings corresponding to the cubic fluorite (F) structure of nanocrystalline ceria, while HREM analysis showed that the nanoparticles had the shape of slightly truncated octahedra (Fig. 2(b)).

Table 1
Properties of different magnetic nanoparticles: size (d_{TEM}), *specific surface area* (BET), and magnetic properties—saturation magnetization (M_S), remanence (M_R), and coercivity ($\mu_0 Hc$).

Sample	d_{TEM} [nm]	BET [m^2/g]	M_S [A·m^2/kg]	M_R [A·m^2/kg]	$\mu_0 Hc$ [mT]
C-IONP	11.2 ± 4.1	150.8	62.3	3.0	2.7
HT-IONP	18.4 ± 4.2	96.1	66.6	5.5	7.2
C-IONP-SIL	/	131.4	31.8	2.6	2.6
HT-IONP-SIL	/	84.6	41.5	6.0	7.4
C–Ru	/	178.2	18.2	0.54	1.4
HT–Ru	/	172.9	19.9	2.4	6.1

When iron–oxide nanoparticles without silica coating (C–IONPs) were suspended in the reaction mixture, the morphology of the precipitated ceria changed. Interestingly, the size of the octahedrally shaped ceria nanocrystallites increased, compared with precipitation without core nanoparticles, to approximately 10 nm. They were present as small (≈40 nm) dense aggregates, always adhered to the iron–oxide nanoparticles (Fig. 3). Within the aggregates, the ceria nanocrystallites were usually oriented in similar crystallographic directions (Fig. 3(b)). Electron diffraction collected from a larger area of the sample showed a pattern composed of diffraction rings corresponding to both the spinel (S) structure of iron oxide and the fluorite (F) structure of ceria (inset of Fig. 3(a)). XRD analysis showed broad peaks corresponding to spinel iron oxide ($d_{XRD} = 15$ nm) and fluorite ceria ($d_{XRD} = 11$ nm) (Fig. SI5).

Only when the iron–oxide nanoparticles were coated with a silica layer prior to deposition did ceria form a continuous shell on the magnetic nanoparticles (Fig. 4). The shell, 3–6 nm thick, was composed of nanocrystallites ≈3 nm in size. In some small regions, the shell was slightly thicker, reaching up to ≈15 nm. The corresponding electron diffraction pattern (inset of Fig. 4(a)) was a combination of sharper diffraction rings from 10 nm iron–oxide nanoparticles with the spinel structure and very diffuse rings corresponding to the fluorite structure. High-resolution STEM imaging showed that the deposited ceria nanocrystallites had a globular shape (Fig. 4(e and f)). Only very broad humps at the positions corresponding to the fluorite structure were visible in the XRD pattern dominated by much larger peaks of the spinel iron oxide (Fig. SI5). The d_{XRD} for ceria crystallites was estimated to be ≈ 3.4 nm.

The composition of the nanocomposite product—i.e., the thickness of the ceria shell—can be tuned by adjusting the Ce^{3+}/C–IONP–SIL mass ratio. For example, when the Ce^{3+}/C–IONP–SIL mass ratio was reduced from 1 to 0.3, the C–IONP–SIL nanoparticles were covered with dispersed ceria nanocrystallites, attached to the silica surfaces either individually or as small aggregates (Fig. 5(a and b)). By increasing the Ce^{3+}/C–IONP–SIL mass ratio to 3, the C–IONP–SIL core nanoparticles could no longer be resolved in the (S)TEM images (Fig. 5(c and d)), as they were covered by a thick deposit of nanocrystalline ceria. The presence of magnetic nanoparticles was detectable only through their response to a magnetic field gradient, as the suspended material was rapidly drawn to a permanent magnet (the material exhibited M_S of 6 A m^2/kg). Morphologically, the material appeared as aggregated globular particles, approximately 50 nm to over 100 nm in size, composed of ≈3 nm ceria nanocrystallites. Assuming that each globular particle contained a single IONP at its centre, the thickness of the ceria shell was estimated to be ≈ 20–50 nm. The thick ceria shell almost completely attenuated the EDXS signal (Fe Kα, Si Kα) originating from the embedded IONP–SIL cores.

3.3. *Influence of different parameters on ceria deposition*

The method used to deposit ceria onto silica-coated magnetic nanoparticles proved to be highly robust. Varying the deposition parameters over a relatively broad range had only a minor influence on the properties of the resulting product. For example, no changes in the nanocomposite structure were detected by TEM when the concentrations of all reactants were increased two-fold or decreased twenty-fold. Moreover, the appearance of the nanocomposite remained essentially unchanged when the amount of HMTA added during deposition was varied. According to TEM analysis, increasing the HMTA/Ce^{3+} molar ratio from the initial value of 2 to 5, or decreasing it to 1, did not significantly affect the nanocomposite structure; however, in both cases, larger micron-sized dendritic crystals of a Ce-rich phase—cerium oxide carbonate hydrate ($Ce_2O(CO_3)_2{\cdot}H_2O$)—were observed in the samples in addition to the nanocomposite (Fig. SI6).

Furthermore, the pH of the reaction suspension had only a minor

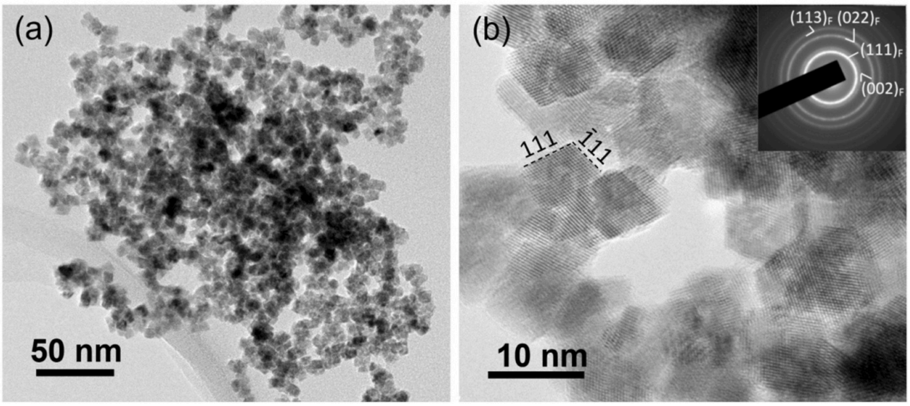

Fig. 2. TEM images (a, b) of ceria nanoparticles. Inset in Figure (b) shows a corresponding electron diffraction pattern indexed according to a fluorite (F) structure.

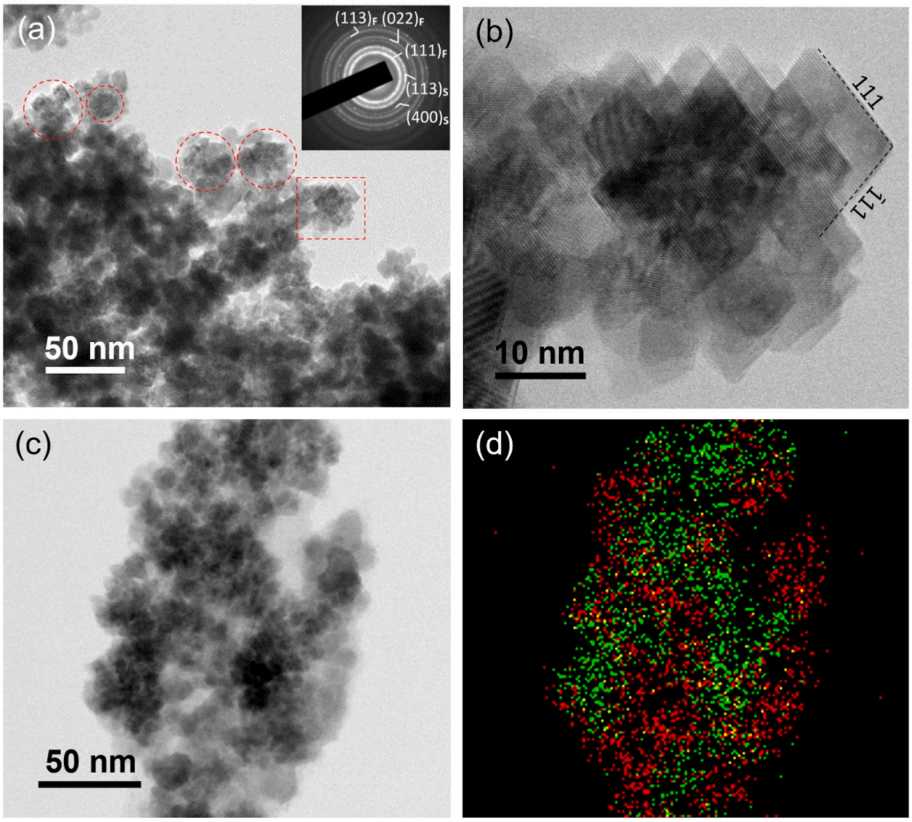

Fig. 3. TEM image (a) of ceria deposited on iron-oxide nanoparticles C–IONP (inset shows a corresponding electron diffraction pattern indexed according to the fluorite (F) structure and the spinel (S) structure). Small aggregates of ceria nanocrystallites are marked with red circles. Figure (b) shows an enlarged area with an aggregate of ceria nanocrystallites marked on Figure (a) with red rectangle. BF STEM image (c) and a corresponding EDXS elemental maps (d) show distribution of Ce (green) and Fe (red). (For interpretation of the references to colour in this figure legend, the reader is referred to the Web version of this article.)

effect on the product morphology. The initial pH of the reaction suspension, before heating, was usually adjusted to 8.0 with aqueous ammonia solution. At a decreased pH of 5.0, the vast majority of ceria still deposited onto the magnetic core nanoparticles; however, some agglomerated ceria nanoparticles not attached to the cores were also present (Fig. SI7). When the pH was increased to 10.0, all of the ceria deposited onto the core nanoparticles; however, the shell was composed of significantly larger ceria nanocrystallites compared with those formed at the usual pH of 8.0 (see Fig. 4). These nanocrystallites exhibited a faceted shape and a size of approximately 5 nm (Fig. 6). At an even higher pH of 11.0, the product became nonhomogeneous, consisting of agglomerated ceria nanoparticles and magnetic nanoparticles covered with aggregates of ceria nanocrystallites.

3.4. Mechanism of ceria shell formation

After standing at room temperature for a prolonged period (>6 h), a white precipitate formed in the aqueous solution of cerium(III) nitrate and HMTA. The formation of a hydrogen-bonded Ce^{3+}–HMTA coordination compound with the formula $[Ce(NO_3)_2(H_2O)_5](HMTA)_2(NO_3)(H_2O)_3$ in aqueous solution has been reported [46,47]. However, XRD analysis of the dried precipitate showed that it consisted of cerium(III) oxide carbonate hydrate ($Ce_2O(CO_3)_2{\cdot}H_2O$). This carbonate most likely formed directly via hydrolysis of cerium(III) nitrate in the presence of

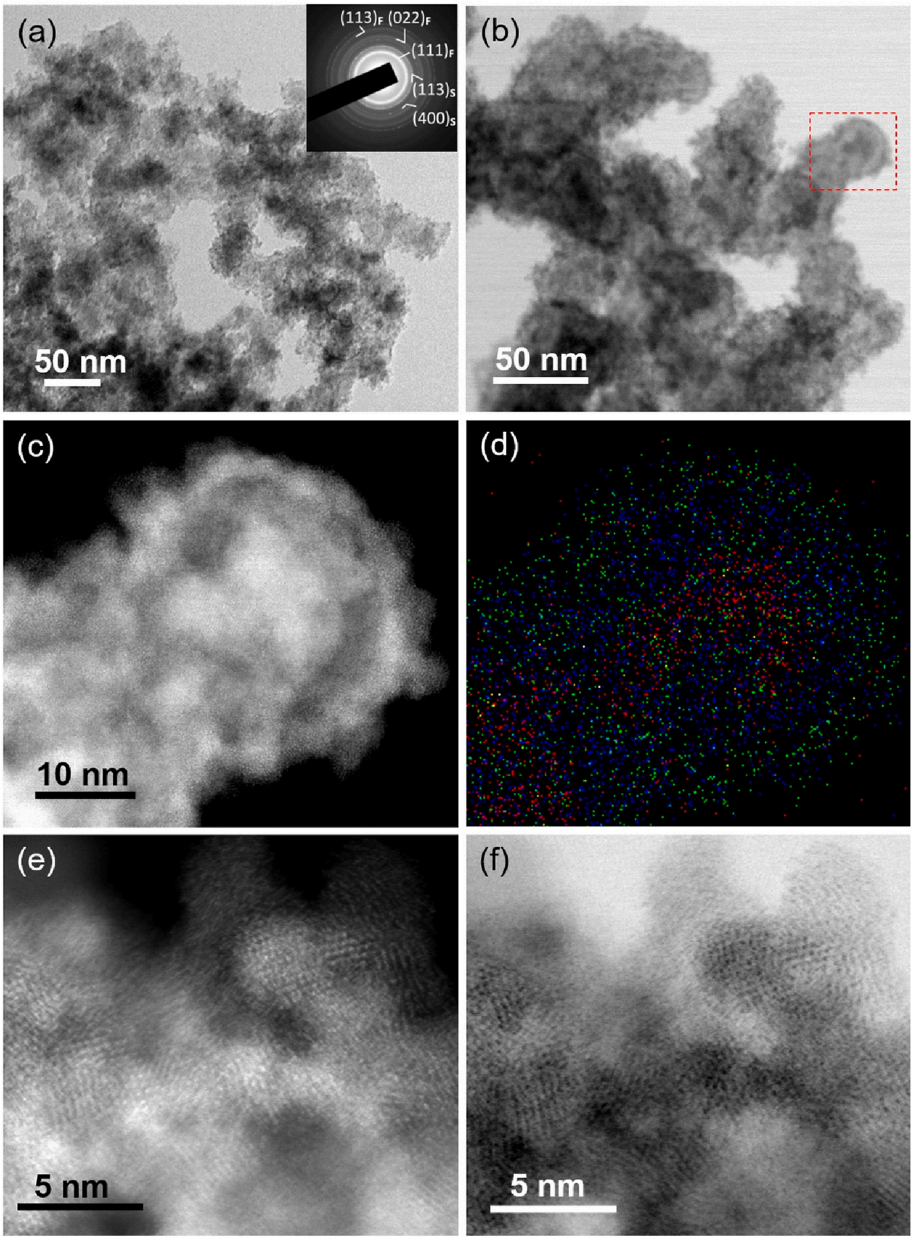

Fig. 4. (a) TEM image of ceria deposited on silica-coated iron-oxide nanoparticles C–IONP–SIL (inset shows a corresponding electron diffraction pattern indexed according to the fluorite (F) structure and spinel (S) structure). (b) BF STEM image of C–IONP–SIL. (c) HAADF STEM image of enlarged area marked on Fig. (b) with red rectangle. (d) A corresponding EDXS elemental maps showing distribution of Ce (green), Fe (red) and Si (blue). (e) HAADF and (f) BF STEM images of ceria deposit at higher magnification. (For interpretation of the references to colour in this figure legend, the reader is referred to the Web version of this article.)

HMTA, followed by reaction with atmospheric CO_2 [47]. HMTA slowly hydrolyses in aqueous solution to yield ammonia and formaldehyde; however, the solution pH remains near 8.0, which is insufficient for the precipitation of cerium(III) hydroxide ($Ce(OH)_3$), that becomes stable only above pH ≈ 10.4 [48,49]. Nevertheless, the transient formation of a Ce^{3+}–HMTA coordination compound cannot be excluded.

Cerium(III) oxide carbonate hydrate was also the only Ce-containing phase detected when ceria deposition was carried out at elevated temperatures below ≈50 °C. Acicular carbonate crystals, several hundred nanometers in length, often assembled into star-like aggregates, were observed together with much smaller core IONPs (Fig. 7(a)). Interestingly, these carbonate crystals were highly sensitive to the electron beam in the TEM. Upon irradiation, they rapidly transformed into nanocrystalline fluorite-structured ceria without any change in particle morphology, indicating in situ oxidation to CeO_2. At 50 °C, individual carbonate particles were still present (Fig. 7(b)), but most Ce had already been deposited as ceria on the core nanoparticles. The irregular, frequently hollow shapes of the remaining carbonate particles suggested that they were dissolving (Fig. 7(b)). Based on these observations, we conclude that cerium(III) oxide carbonate hydrate begins to form already at room temperature. At temperatures approaching 50 °C, Ce^{3+} in the precipitated carbonate begins to dissolve and oxidize, leading to the formation of ceria. The slow dissolution and/or oxidation maintains a low supersaturation, enabling exclusively heterogeneous nucleation of ceria on the surfaces of core nanoparticles present in the reaction mixture.

To further test this mechanism, ceria was deposited onto IONPs by direct oxidation of preformed cerium(III) oxide carbonate hydrate (without HMTA) in parallel experiments. The IONPs and carbonate powder were suspended in water and heated at 50–80 °C under pH

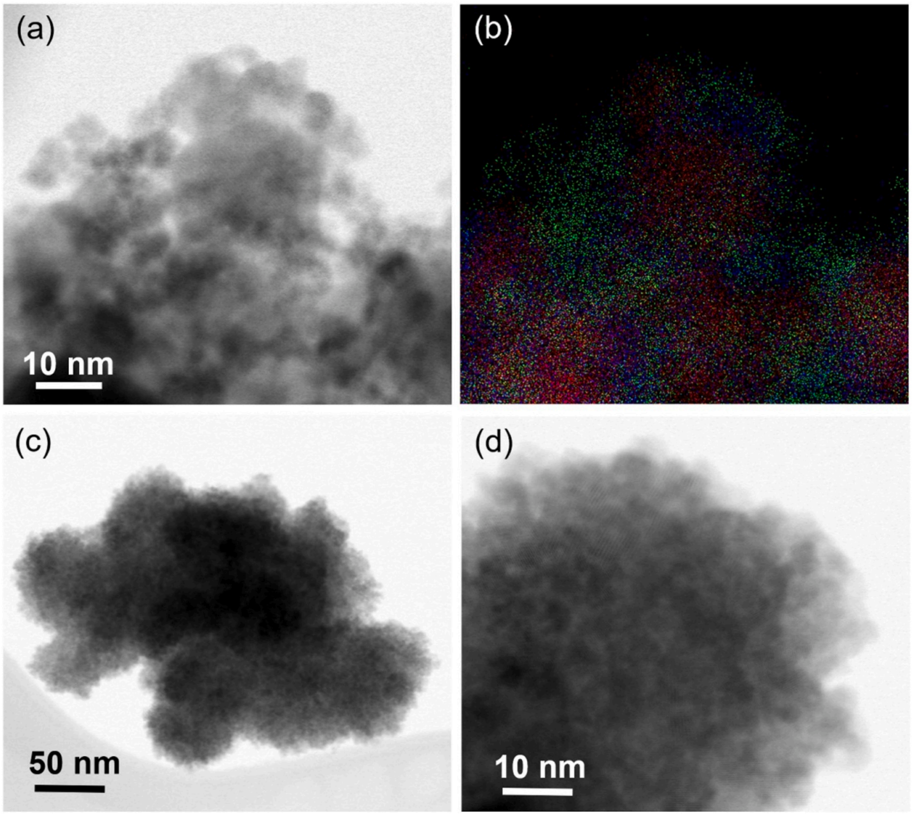

Fig. 5. (a) BF STEM image of nanocomposite synthesized by depositing ceria onto silica-coated iron-oxide nanoparticles at a reduced Ce^{3+}/C-IONP-SIL ratio of 0.3. (b) A corresponding EDXS elemental maps showing the distribution of Ce (green), Fe (red) and Si (blue). (c, d) BF STEM images of the nanocomposite synthesized at ceria at an increased Ce^{3+}/C–IONP–SIL ratio of 3. (For interpretation of the references to colour in this figure legend, the reader is referred to the Web version of this article.)

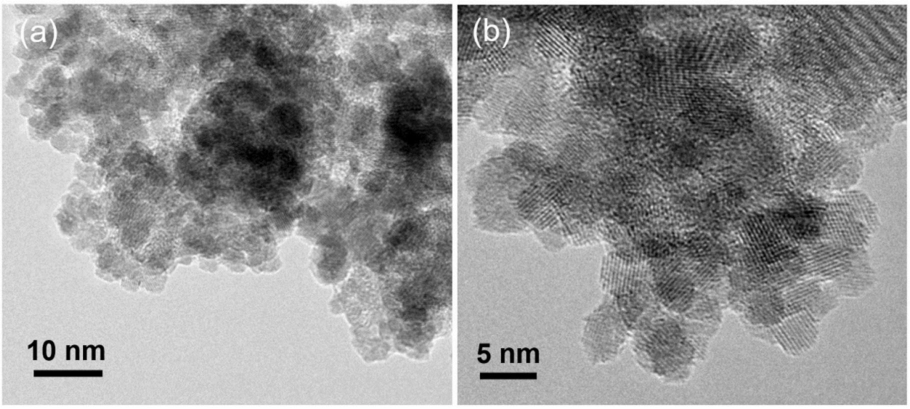

Fig. 6. TEM images of ceria shell deposited onto silica-coated iron-oxide nanoparticles at pH of 10.0.

values ranging from 3 to 10. At temperatures below 70 °C, the carbonate partially dissolved and ceria deposited on the IONPs. Similar to the deposition of ceria in the presence of HMTA, the ceria formed as small aggregates of larger crystallites directly on the iron–oxide cores (Fig. SI8) and as a continuous shell on the silica-coated nanoparticles (Fig. SI9). However, the amount of deposited ceria remained relatively low and could not be effectively controlled at any tested pH value. At temperatures above 70 °C, the large carbonate crystals topotactically transformed into nanocrystalline ceria (see the SI for details).

These parallel experiments confirmed the proposed deposition mechanism involving the intermediate formation of cerium(III) oxide carbonate hydrate. The relatively slow oxidation and/or dissolution of the carbonate particles above ≈50 °C maintains a low supersaturation of the precipitating ceria, which is key to understanding the observed differences in nanocrystallite shape and size.

Ce^{3+} precipitation in the presence of HMTA without core nanoparticles yielded ≈5 nm ceria particles with truncated octahedral shapes (Fig. 2). Under identical synthesis conditions, ceria deposited as small aggregates of ≈10 nm octahedral nanocrystallites directly onto iron–oxide nanoparticles (Fig. 3), and as a continuous shell of ≈3 nm nanocrystallites when the iron–oxide nanoparticles were coated with silica (Fig. 4). The variation in particle shape likely reflects the size-dependent transition from nearly spherical forms of very small crystallites to more defined crystal geometries as they grow. To minimize surface energy,

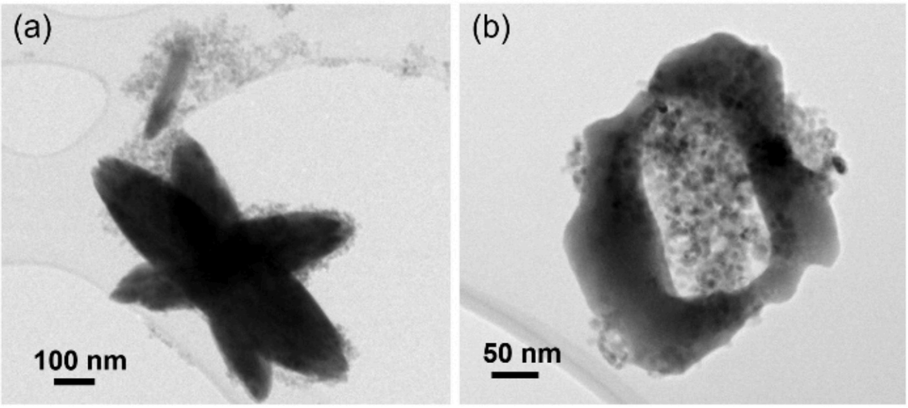

Fig. 7. TEM images of cerium(III) oxide carbonate hydrate particles mixed with the C-IONPs after ceria-deposition reaction conducted for 2 h at 45 °C (a) and at 50 °C (b).

very small nanocrystallites adopt a near-spherical (globular) morphology, since a sphere minimizes surface area for a given volume. As the crystallites grow, differences in surface energies between crystal facets become significant, leading to the appearance of faceted shapes. In ceria, the {111} surfaces exhibit the lowest surface energy, favouring the formation of octahedral nanocrystals during slow growth [50].

The observed differences in nanoparticle size can be explained by variations in the rates of nucleation and growth of ceria crystallites, following the classical LaMer model [51]. At higher supersaturation, rapid nucleation generates a greater number of nuclei, resulting in smaller particles. The minimal supersaturation required for nucleation is determined by the surface energy of the forming nucleus. Because the liquid–solid interfacial energy is generally higher than the solid–solid interfacial energy, homogeneous nucleation (i.e., nucleation in the absence of core nanoparticles) occurs at higher supersaturation than heterogeneous nucleation, leading to the formation of smaller particles.

During heterogeneous nucleation, the nucleation threshold depends on the interfacial energy between the precipitating solid and the substrate. Iron oxide (maghemite) exhibits a much higher surface energy (≈ 1.9 J/m^2) [52] than silica (≈ 0.34 J/m^2) [53]. Nucleation of ceria on maghemite therefore begins at much lower supersaturation than on silica, producing a relatively small number of nuclei. Because the oxidation and/or dissolution of the carbonate particles proceeds slowly, supersaturation remains low, and the available precursor is preferentially consumed for the growth of existing nuclei. Such slow growth under low supersaturation promotes (i) the formation of the equilibrium octahedral shape of the nanocrystallites [50] and (ii) oriented-attachment (coalescence) growth—a common growth mechanism for the ceria [54]—both evident in Fig. 3. Moreover, heterogeneous nucleation on maghemite may depend on the availability of specific nucleation sites—for example, certain crystal facets on the roughly spherical nanoparticles. In contrast, on isotropic, amorphous silica, nucleation occurs at higher supersaturation and proceeds rapidly and continuously across the surface. Under such conditions, most of the precipitated ceria is consumed during nucleation, resulting in minimal growth and the formation of a continuous shell of small nanocrystallites.

3.5. *Deposition of catalytic Ru nanoparticles onto the magnetic ceria supports*

Two magnetic catalysts, C–Ru and HT–Ru, were prepared by deposition of catalytic Ru nanoparticles onto the magnetic ceria supports containing C–IONP–SIL and HT–IONP–SIL magnetic nanoparticles, respectively. Fig. 8 shows STEM images of the HT–Ru composite with the corresponding EDXS elemental maps. EDXS at lower magnifications (Fig. 8(a–d)) showed the Ru signal coming from the entire area of the nanocomposite, suggesting homogeneous distribution of the Ru over the magnetic support. With combining HAADF imaging and EDXS mapping very small globular Ru nanoparticles, 1–2 nm in size (marked with yellow circles on the HAADF STEM image Fig. 8(e and f)), were resolved on the ceria surfaces at higher magnification.

XRF analyses showed that the magnetic catalysts C–Ru and HT–Ru contained 2.1 wt% and 1.4 wt% of Ru, respectively. Because of the smaller C–IONP–SIL core nanoparticles the catalyst C–Ru exhibited somewhat larger specific surface area (178.2 m^2/g) compared to the HT–Ru containing larger HT–IONP–SIL core nanoparticles (172.9 m^2/g) as measured via BET method (Table 1).

3.6. *Magnetic properties and heating ability*

To evaluate the heating potential of the prepared catalysts, room-temperature static and dynamic magnetization curves were recorded (Fig. 9). Both catalysts, C–Ru (containing co-precipitated iron–oxide nanoparticles, C–IONPs, ≈11 nm in size) and HT–Ru (containing hydrothermally-treated iron–oxide nanoparticles, HT–IONPs, ≈18 nm in size), exhibited narrow hysteresis loops characteristic of magnetically soft materials (Fig. 9(a)). Ceria coating reduced the saturation magnetization (M_S) to 18.2 and 19.9 A m^2/kg for the C–Ru and HT–Ru catalysts, respectively (Table 1). The mass fractions of magnetic iron oxide were determined to be 27.1 ± 3.7 wt% for C–Ru and 32.2 ± 3.6 wt% for HT–Ru. Correspondingly, the normalized saturation magnetizations are 67.5 ± 9.2 A m^2/kg$_{\mathrm{IONP}}$ and 62.2 ± 7.0 A m^2/kg$_{\mathrm{IONP}}$ for the C–Ru and HT–Ru catalysts, respectively. These normalized values are close to the saturation magnetizations of the C–IONP and HT–IONP starting materials, indicating that the magnetic properties of the iron-oxide cores remained intact after coating. The observed reduction in the unnormalized M_S of the catalysts can therefore be attributed to dilution by the diamagnetic silica, ceria, and ruthenium phases.

Because the magnetic IONPs are immobilized within the nanocomposite catalysts, Brownian relaxation can be excluded as a heating mechanism under AMF. The evolution of dynamic magnetization loops as a function of AMF amplitude was measured for the C–Ru and HT–Ru (Fig. 9(b and c)). Despite their nearly identical static magnetization loops, their dynamic behaviour differed markedly. The C–Ru catalyst exhibited relatively narrow dynamic loops that, above an AMF amplitude of ≈25 mT, began to approach saturation. This effect is more clearly seen in the dependence of the specific absorption rate (SAR = frequency × area of the dynamic loop) on AMF amplitude (Fig. 9(d)). In contrast, HT–Ru, which contains the larger HT–IONPs, displayed elliptical dynamic magnetization curves across all AMF amplitudes (Fig. 9(c)). The SAR of HT–Ru increased nonlinearly in the 5–35 mT range, indicating that the HT–IONPs remained far from saturation.

In both catalysts, the iron oxide cores are in the ferromagnetic regime (Fig. 9(a) and Table 1), where the Stoner–Wohlfarth-derived model can

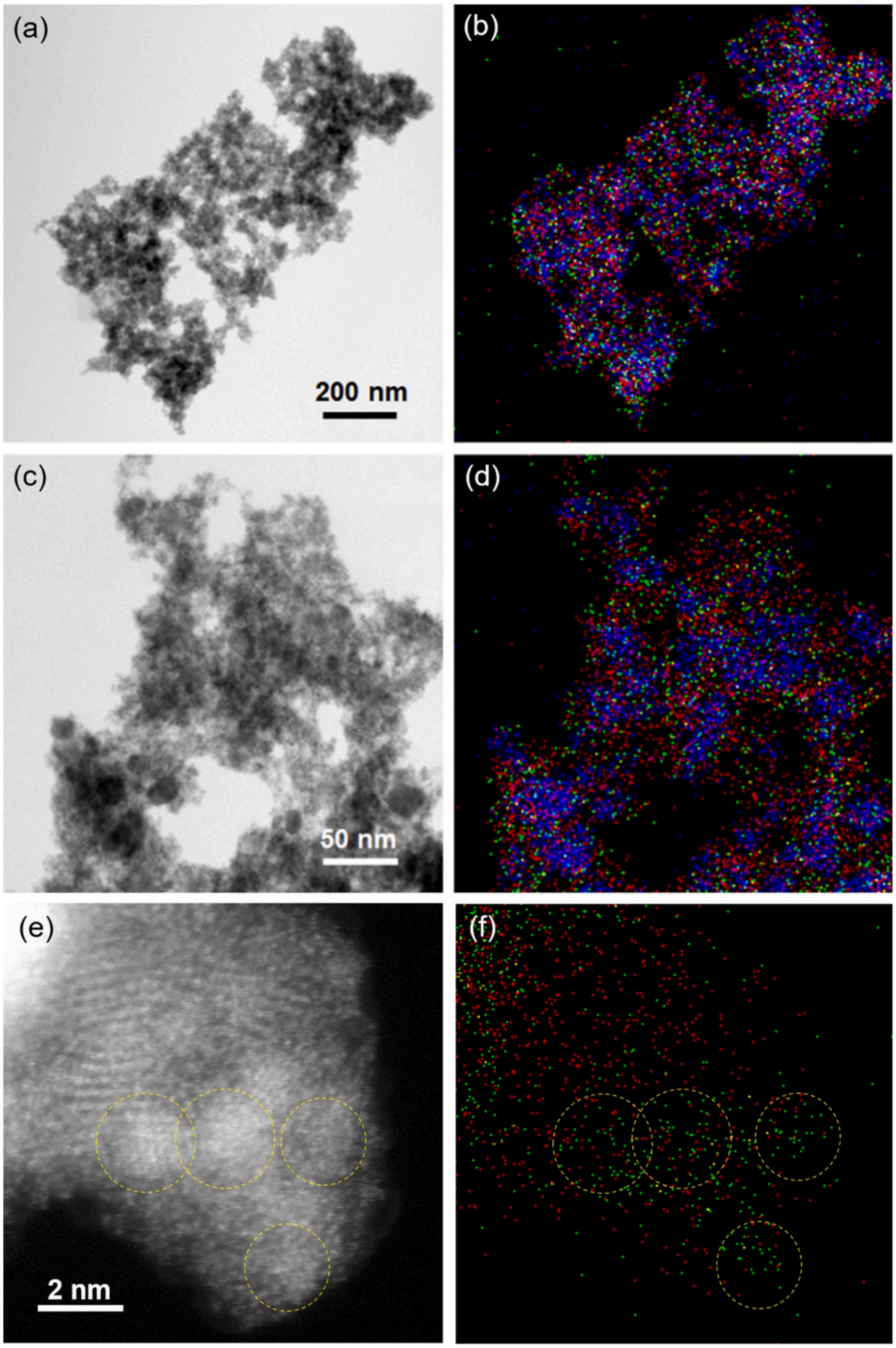

Fig. 8. BF (a, c) and HAADF (e) STEM images with corresponding EDXS elemental maps (b, d, f) showing distribution of Ce (red), Fe (blue) and Ru (green) on magnetic catalyst HT–Ru synthesized by precipitation of Ru nanoparticles onto a ceria support containing HT–IONP–SIL magnetic nanoparticles. Ru NPs are marked with yellow circles on Figs. (e, f). (For interpretation of the references to colour in this figure legend, the reader is referred to the Web version of this article.)

qualitatively describe the observed differences in dynamic magnetization behaviour [55–57]. The area of the dynamic loop depends on intrinsic magnetic parameters such as saturation magnetization, anisotropy energy barrier (which increases with particle size), and AMF amplitude. For ferromagnetic nanoparticles of the same composition, the loop area is small at AMF amplitudes below the coercive field ($\mu_0 H_C$), increasing with a power-law dependence above $\mu_0 H_C$ and saturating only at fields well above this value [55,56,58]. Because $\mu_0 H_C$ is size-dependent, smaller ferromagnetic nanoparticles exhibit higher SAR values than larger ones at low-field amplitudes; however, their SAR saturates at lower amplitudes and reaches a smaller maximum value [57].

The evolution of SAR with AMF amplitude for the two catalysts follows this characteristic behaviour. The smaller ≈11 nm C–IONPs (in C–Ru) exhibited slightly higher SAR values than the ≈18 nm HT–IONPs (in HT–Ru) at fields below 15 mT, consistent with their softer magnetic character, as reflected by their low coercive field ($\mu_0 H_C = 1.3$ mT). At higher field amplitudes, the SAR of the magnetically harder HT–Ru catalyst ($\mu_0 H_C = 6.1$ mT) surpassed that of C–Ru. Dynamic magnetization curves indicate that the smaller C–IONPs begin to approach saturation at ≈15 mT, whereas the larger HT–IONPs retain elliptical hysteresis loops and remain far from saturation even at 35 mT. Static

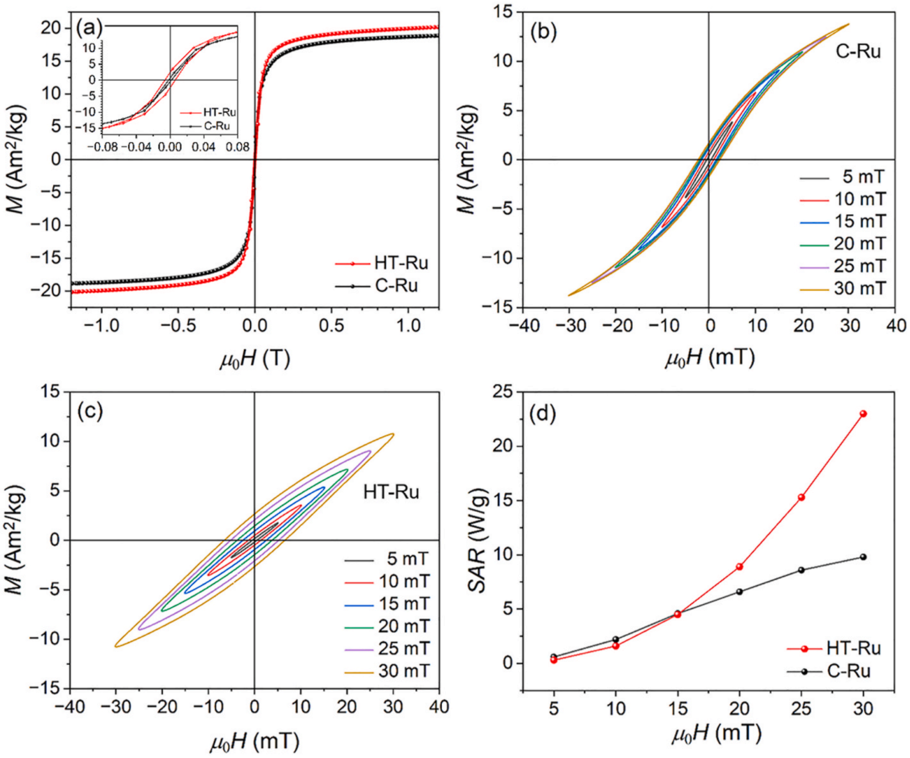

Fig. 9. Magnetic properties of the catalysts C–Ru and HT–Ru: (a) room-temperature static magnetization curves; (b, c) dynamic magnetization curves as a function of magnetic-field amplitude; and (d) specific absorption rate as a function of magnetic field amplitude. All dynamic hysteresis loops and SAR values are at 112 kHz.

magnetization loops show that both samples reach ~90 % of M_S at ≈255 mT— well above 15 mT— indicating no significant difference in static saturation fields (Fig. 9(a)). Under dynamic conditions, however, the magnetization of HT–IONPs is consistently lower than that of C–IONPs at identical AMF amplitudes, consistent with their magnetically harder character arising from their larger size and correspondingly longer relaxation times.

The steady-state temperature of the reaction mixture depends not only on the amount and heating power of the magnetic catalyst, but also on the overall thermal balance of system. A simple test was performed to evaluate the heating efficiency of the catalysts. Each catalyst (1.5 g) was dispersed in 40 mL of water and stirred using a glass overhead stirrer. The beaker was placed inside the magnetic coil, and an N-type thermocouple was used to continuously monitor the temperature. An AMF with an amplitude of 38 mT and frequency of 112 kHz was applied to assess heating performance.

For the C–Ru catalyst, the water temperature increased slowly, reaching a steady-state value of 40 °C after 10 min, indicating relatively low heating efficiency. In contrast, the HT–Ru suspension reached 90 °C within 20 min, demonstrating significantly higher heating capability.

3.7. Testing of catalytic activity

The developed HT–Ru catalyst was evaluated for its activity, selectivity, and stability in the magnetically heated hydrogenation of the bio-based compound 5-(hydroxymethyl)furfural (HMF). HMF is typically obtained via acid-catalysed dehydration of fructose or glucose, or by hydrolysis and dehydration of polysaccharides [3]. Through intermediate catalytic hydrogenation to 2,5-bis(hydroxymethyl)furan (BHMF), HMF can be further valorised into several economically important chemicals, among which 2,5-di(hydroxymethyl)tetrahydrofuran (DHMTHF) and 2,5-dimethylfuran (DMF) are particularly attractive [59,60]. Because HMF contains both aldehyde and hydroxyl functional groups, it is prone to self-condensation under acidic or basic conditions, forming oligomers and humins that are unreactive toward valorisation and can deactivate hydrogenation catalysts [61,62]. Selective hydrogenation of HMF to the more stable diol BHMF is therefore an attractive pathway. BHMF is resistant to self-condensation, is used in the production of polyurethane foams and polyesters, and can be further hydrogenated to value-added chemicals [3,63,64].

Hydrogenation of HMF under magnetic heating was performed in a quartz pressure vessel equipped with a Teflon Rushton turbine, a thermocouple, and a sampling line allowing periodic collection of the reactor contents (Fig. 1). All components placed within the AMF-generating coil were made of quartz or Teflon, ensuring that they did not heat under the AMF. The observed temperature rise in the reactor was therefore solely due to magnetic heating of the catalyst.

Using an AMF amplitude of 38 mT, the temperature of the reaction medium containing dispersed HT–Ru catalyst increased to 150 °C within 15 min (Fig. 10(a)). The higher steady-state temperature compared with the preliminary tests in water can be attributed to the lower heat capacity of THF, which is approximately half that of water. In contrast, under the same AMF conditions, the magnetic catalyst C–Ru was unable to heat the reaction mixture to temperatures sufficient for HMF hydrogenation. Hydrogenation of bio-based compounds over Ru-based catalysts typically requires temperatures well above 60 °C [3].

Consequently, HMF hydrogenation was carried out using only the HT–Ru catalyst. The concentration of HMF began to decrease during the heating stage and continued to decline steadily until complete conversion to BHMF was achieved after approximately 200 min at 150 °C (Fig. 10(a)). After the reaction, the system was allowed to cool naturally to room temperature, and the catalyst was recovered magnetically, washed several times with fresh THF, and reused to evaluate its stability (Fig. 10(b)). Conversions and selectivities were compared at 20 min, where conversions were low and the kinetic regime can be assumed, and at 80 min, where conversions were substantially higher. In both cases, the conversions remained nearly constant across multiple reuse cycles (Fig. 10(b)). In all experiments, complete conversion and 100 % selectivity to BHMF were achieved after 200 min, demonstrating the excellent stability of the HT–Ru catalyst during magnetically induced

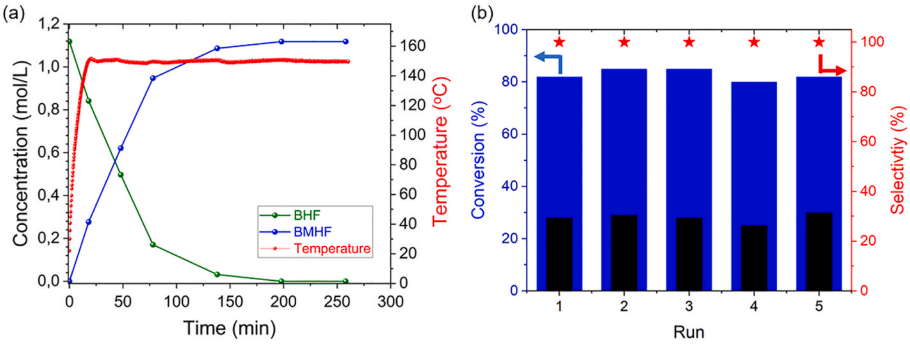

Fig. 10. The effect of reaction time on BHF reactant and BHMF product distribution (a) and recycling (b) of the HT–Ru catalyst under AMF heating at amplitude of 38 mT and frequency of 112 kHz. Blue bars correspond to conversions measured at 80 min, while black bars correspond to conversions measured at 20 min. (For interpretation of the references to colour in this figure legend, the reader is referred to the Web version of this article.)

hydrogenation of HMF to BHMF.

The catalytic performance of HT–Ru under magnetic heating (150 °C, 1 MPa H_2) was compared with literature data obtained under conventional and magnetic heating.

Pomeroy et al. reported HMF hydrogenation over various Ni/activated carbon catalysts in a conventionally heated slurry reactor using THF as the solvent [65]. Their systems exhibited lower HMF conversions than the HT–Ru catalyst; even at higher temperature and pressure (170 °C, 5 MPa H_2), complete conversion was not achieved within 6 h. Moreover, BHMF selectivity decreased due to the formation of (5-methyl-2-furyl)methanol and 2,5-bis(hydroxymethyl)tetrahydrofuran, attributed to excessive hydrogen pressure [65]. The same group later investigated an alumina-supported Ni/Ce catalyst, achieving 96 % BHMF selectivity at 140 °C and 5 MPa H_2 using a THF/water solvent mixture [66]. Alamillo et al. employed a ceria-supported Ru catalyst at 130 °C and ~2.8 MPa H_2, obtaining an 84 % BHMF yield after 2 h [67].

In the case of magnetically heated hydrogenation, Gyergyek et al. demonstrated that Ru supported on magnetic carbon (iron oxide encapsulated within a carbon matrix) was active for HMF hydrogenation in the green solvent *n*-butanol; however, BHMF selectivity decreased due to the acidic surface properties of the carbon support, which promoted the formation of di-, tri-, and oligomeric by-products [19]. $FeNi_3$ nanoparticles supported on Ni were also highly active for HMF hydrogenation under magnetic heating, although no BHMF could be isolated because over-hydrogenation proceeded at a significant rate [68].

In comparison, our HT–Ru catalyst achieved ~94 % BHMF yield after 2 h and 100 % yield after 3 h at 150 °C and only 1 MPa H_2, demonstrating high activity and selectivity under relatively mild reaction conditions.

4. Conclusions

Ru nanocatalysts supported on nanocrystalline ceria with embedded magnetic iron–oxide nanoparticles (IONPs) were synthesized for use in catalysis by magnetic heating. The magnetic catalyst supports were prepared by depositing ceria onto IONPs via controlled precipitation of Ce^{3+} ions in the presence of hexamethylenetetramine (HMTA) in aqueous suspension. Ceria was deposited onto globular IONPs of two different sizes — ≈11 nm (co-precipitated at room temperature) and ≈18 nm (hydrothermally-treated at 120 °C) — both before and after coating with a thin layer of silica.

When uncoated IONPs were used as core particles, ceria formed as small aggregates of octahedrally shaped crystallites (≈10 nm) attached to the IONPs. A continuous, homogeneous nanocrystalline ceria shell (≈3 nm crystallites) was obtained only when silica-coated IONPs were used. Mechanistic analysis revealed an important role for cerium(III) oxide carbonate hydrate as an intermediate in ceria formation.

After deposition of catalytic Ru nanoparticles (1–2 nm) onto the magnetic ceria supports, the resulting catalysts were evaluated for their magnetic heating performance and catalytic activity. At lower field amplitudes (<15 mT), catalysts prepared with both sizes of IONPs exhibited comparable specific absorption rates ($SAR_{15mT} \approx 5$ W/g), as determined from dynamic magnetization measurements. However, at higher amplitudes, the larger IONPs showed significantly improved heating efficiency, with $SAR_{30mT} \approx 30$ W/g compared to ≈10 W/g for the smaller, co-precipitated IONPs.

Testing in the magnetically-heated hydrogenation of the bio-based compound 5-(hydroxymethyl)furfural (HMF) to 2,5-bis(hydroxymethyl)furan (BHMF) demonstrated high catalytic activity, 100 % selectivity, and excellent stability upon recycling.

CRediT authorship contribution statement

Nina Križaj Kosi: Writing – review & editing, Writing – original draft, Methodology, Investigation. **Jakov-Stjepan Pavelić:** Methodology, Investigation. **Miha Grilc:** Writing – review & editing, Writing – original draft, Supervision, Methodology, Conceptualization. **Sašo Gyergyek:** Writing – review & editing, Writing – original draft, Validation, Methodology, Conceptualization. **Darko Makovec:** Writing – review & editing, Writing – original draft, Validation, Supervision, Resources, Project administration, Methodology, Investigation, Funding acquisition, Formal analysis, Conceptualization.

Declaration of competing interest

The authors declare that they have no known competing financial interests or personal relationships that could have appeared to influence the work reported in this paper.

Acknowledgements

The authors acknowledge the financial support from the Slovenian Research Agency (ARIS) for research core funding No. P2-0089. The authors thank Ž. Trošt and Š. Pok for help in the laboratory, and A. Sedminek and A. Pečkaj for help with catalytic testing.

Appendix A. Supplementary data

Supplementary data to this article can be found online at https://doi.org/10.1016/j.jpcs.2026.113517.

Data availability

Data will be made available on request.

References

[1] G. Papanikolaou, G. Centi, S. Perathoner, P. Lanzafame, Catalysis for e -Chemistry: need and Gaps for a Future De-Fossilized Chemical Production, with Focus on the Role of Complex (Direct) Syntheses by Electrocatalysis, ACS Catal. 12 (2022) 2861–2876, https://doi.org/10.1021/acscatal.2c00099.

[2] J.L. Barton, Electrification of the chemical industry, Science 368 (2020) 1181–1182, https://doi.org/10.1126/science.abb8061.

[3] M. Besson, P. Gallezot, C. Pinel, Conversion of biomass into chemicals over metal catalysts, Chem. Rev. 114 (2014) 1827–1870, https://doi.org/10.1021/cr4002269.

[4] W. Wang, G. Tuci, C. Duong-Viet, Y. Liu, A. Rossin, L. Luconi, J.-M. Nhut, L. Nguyen-Dinh, C. Pham-Huu, G. Giambastiani, Induction heating: an enabling technology for the heat management in catalytic processes, ACS Catal. 9 (2019) 7921–7935, https://doi.org/10.1021/acscatal.9b02471.

[5] J. Mazarío, S. Ghosh, V. Varela-Izquierdo, L.M. Martínez-Prieto, B. Chaudret, Magnetic nanoparticles and radio frequency induction: from specific heating to magnetically induced catalysis, ChemCatChem 17 (2025), https://doi.org/10.1002/cctc.202400683.

[6] A. Bordet, W. Leitner, B. Chaudret, Magnetically induced catalysis: definition, advances, and potential, Angew. Chemie Int. Ed. 64 (2025), https://doi.org/10.1002/anie.202424151.

[7] J.-S. Pavelić, S. Gyergyek, B. Likozar, M. Grilc, Process electrification by magnetic heating of catalyst, Chem. Eng. J. 505 (2025) 158928, https://doi.org/10.1016/j.cej.2024.158928.

[8] Z.J. Díaz-Puerto, Á. Raya-Barón, P.W.N.M. van Leeuwen, J.M. Asensio, B. Chaudret, Determination of the surface temperature of magnetically heated nanoparticles using a catalytic approach, Nanoscale 13 (2021) 12438–12442, https://doi.org/10.1039/D1NR02283K.

[9] J.M. Asensio, A.B. Miguel, P. Fazzini, P.W.N.M. van Leeuwen, B. Chaudret, Hydrodeoxygenation using magnetic induction: high-temperature heterogeneous catalysis in solution, Angew. Chemie Int. Ed. 58 (2019) 11306–11310, https://doi.org/10.1002/anie.201904366.

[10] S. Gyergyek, M. Grilc, B. Likozar, D. Makovec, Electro-hydrogenation of biomass-derived levulinic acid to γ-valerolactone via the magnetic heating of a Ru nanocatalyst, Green Chem. 24 (2022) 2788–2794, https://doi.org/10.1039/D2GC00102K.

[11] C.L. Roman, N. da Silva Moura, S. Wicker, K.M. Dooley, J.A. Dorman, Induction heating of magnetically susceptible nanoparticles for enhanced hydrogenation of oleic acid, ACS Appl. Nano Mater. 5 (2022) 3676–3685, https://doi.org/10.1021/acsanm.1c04351.

[12] Á. Raya-Barón, J. Mazarío, G. Mencia, P. Fazzini, B. Chaudret, L-Lysine stabilized FeNi nanoparticles for the catalytic reduction of biomass-derived substrates in water using magnetic induction, ChemSusChem 16 (2023), https://doi.org/10.1002/cssc.202300009.

[13] V. Varela-Izquierdo, I. Mustieles-Marín, P. Fazzini, G. Mencía, S. Guelen, R. Rachet, B. Chaudret, Magnetically induced amination of alcohols using MNi@Cu (M=Fe, co) nanoparticles as catalysts, Angew. Chemie Int. Ed. 63 (2024), https://doi.org/10.1002/anie.202412421.

[14] F. Quiroga-Suavita, V. Varela-Izquierdo, T. Hungria, D. Alloyeau, N. Ratel-Ramond, S. Cayez, R.D. Tilley, E.A. Baquero, B. Chaudret, L.-M. Lacroix, Icosahedra CoPd bimetallic nanoparticles for magnetically induced aromatic ketone hydrodeoxygenation, Chem. Mater. 37 (2025) 2762–2771, https://doi.org/10.1021/acs.chemmater.4c03359.

[15] S. Ceylan, C. Friese, C. Lammel, K. Mazac, A. Kirschning, Inductive heating for organic synthesis by using functionalized magnetic nanoparticles inside microreactors, Angew. Chemie Int. Ed. 47 (2008) 8950–8953, https://doi.org/10.1002/anie.200801474.

[16] S. Ceylan, L. Coutable, J. Wegner, A. Kirschning, Inductive heating with magnetic materials inside flow reactors, Chem. Eur J. 17 (2011) 1884–1893, https://doi.org/10.1002/chem.201002291.

[17] J. Hartwig, S. Ceylan, L. Kupracz, L. Coutable, A. Kirschning, Heating under high-frequency inductive conditions: application to the continuous synthesis of the Neurolepticum Olanzapine (Zyprexa), Angew. Chemie Int. Ed. 52 (2013) 9813–9817, https://doi.org/10.1002/anie.201302239.

[18] T. Zanette, A. García-Zaragoza, J. Mazarío, J. Santiago Martinez, B. Chaudret, C. Cerezo-Navarrete, P. Oña-Burgos, Carbon-encapsulated FeNi nanoparticles for efficient magnetically induced levulinic acid hydrogenation, Green Chem. 27 (2025) 11438–11454, https://doi.org/10.1039/D5GC03853G.

[19] S. Gyergyek, A. Kocjan, M. Grilc, B. Likozar, B. Hočevar, D. Makovec, A hierarchical Ru-bearing alumina/magnetic iron-oxide composite for the magnetically heated hydrogenation of furfural, Green Chem. 22 (2020) 5978–5983, https://doi.org/10.1039/D0GC00966K.

[20] S. Lin, W. Hetaba, B. Chaudret, W. Leitner, A. Bordet, Copper-decorated iron carbide nanoparticles heated by magnetic induction as adaptive multifunctional catalysts for the selective hydrodeoxygenation of aldehydes, Adv. Energy Mater. 12 (2022), https://doi.org/10.1002/aenm.202201783.

[21] C. Cerezo-Navarrete, I.M. Marin, H. García-Miquel, A. Corma, B. Chaudret, L. M. Martínez-Prieto, Magnetically induced catalytic reduction of biomass-derived oxygenated compounds in water, ACS Catal. 12 (2022) 8462–8475, https://doi.org/10.1021/acscatal.2c01696.

[22] C. Niether, S. Faure, A. Bordet, J. Deseure, M. Chatenet, J. Carrey, B. Chaudret, A. Rouet, Improved water electrolysis using magnetic heating of FeC–Ni core–shell nanoparticles, Nat. Energy 3 (2018) 476–483, https://doi.org/10.1038/s41560-018-0132-1.

[23] P.M. Mortensen, J.S. Engbæk, S.B. Vendelbo, M.F. Hansen, M. Østberg, Direct hysteresis heating of catalytically active Ni–Co nanoparticles as steam reforming catalyst, Ind. Eng. Chem. Res. 56 (2017) 14006–14013, https://doi.org/10.1021/acs.iecr.7b02331.

[24] P.E. Mortensen, P.M. Ostberg, M. Nielsen, Induction heating of endothermic reactions. https://patentimages.storage.googleapis.com/8a/1d/b8/fe050d2671ff73/WO2017036794A9.pdf, 2017.

[25] A. Meffre, B. Mehdaoui, V. Connord, J. Carrey, P.F. Fazzini, S. Lachaize, M. Respaud, B. Chaudret, Complex nano-objects displaying both magnetic and catalytic properties: a proof of concept for magnetically induced heterogeneous catalysis, Nano Lett. 15 (2015) 3241–3248, https://doi.org/10.1021/acs.nanolett.5b00446.

[26] A. Bordet, L.-M. Lacroix, P.-F. Fazzini, J. Carrey, K. Soulantica, B. Chaudret, Magnetically induced continuous CO2 hydrogenation using composite iron carbide nanoparticles of exceptionally high heating power, Angew. Chemie 55 (2016) 16126–16130, https://doi.org/10.1002/ange.201609477.

[27] S.S. Kale, J.M. Asensio, M. Estrader, M. Werner, A. Bordet, D. Yi, J. Marbaix, P.-F. Fazzini, K. Soulantica, B. Chaudret, Iron carbide or iron carbide/cobalt nanoparticles for magnetically-induced CO2 hydrogenation over Ni/SiRAlOx catalysts, Catal. Sci. Technol. 9 (2019) 2601–2607, https://doi.org/10.1039/C9CY00437H.

[28] B. Rivas-Murias, J.M. Asensio, N. Mille, B. Rodríguez-González, P. Fazzini, J. Carrey, B. Chaudret, V. Salgueiriño, Magnetically induced CO2 methanation using exchange-coupled spinel ferrites in cuboctahedron-shaped nanocrystals, Angew. Chemie Int. Ed. 59 (2020) 15537–15542, https://doi.org/10.1002/anie.202004908.

[29] V. Poletto Dotsenko, M. Bellusci, A. Masi, D. Pietrogiacomi, F. Varsano, Improving the performances of supported NiCo catalyst for reforming of methane powered by magnetic induction, Catal. Today 418 (2023) 114049, https://doi.org/10.1016/j.cattod.2023.114049.

[30] C. Cerezo-Navarrete, I.M. Marin, C. Marini, B. Chaudret, L.M. Martínez-Prieto, Structural transformation of carbon-encapsulated core-shell CoNi nanoparticles during magnetically induced CO2 reduction into CO, Appl. Catal. B Environ. Energy 347 (2024) 123780, https://doi.org/10.1016/j.apcatb.2024.123780.

[31] R. Zhang, X. Liu, N. Song, J. He, Z. Cen, C. Li, M. Wang, H. Tang, W. Liu, X. Ren, D. Ma, Magnetic induction heating-driven rapid cold start of ammonia decomposition for hydrogen production, J. Am. Chem. Soc. 146 (2024) 28635–28641, https://doi.org/10.1021/jacs.4c10851.

[32] H. Chen, J. Lee, Y. Zheng, Q. Duan, A non-traditional energy transfer process in CWPO heterogeneous reaction for wastewater treatment, Chem. Eng. Res. Des. 114 (2016) 142–147, https://doi.org/10.1016/j.cherd.2016.08.020.

[33] Ž. Ponikvar, A. Sedminek, J. Teržan, L. Skubic, Ž. Lavrič, M. Huš, M. Grilc, B. Likozar, D. Makovec, S. Gyergyek, Electrified dynamically responsive ammonia decomposition to hydrogen based on magnetic heating of a Ru nanocatalyst, ChemSusChem 18 (2025), https://doi.org/10.1002/cssc.202401970.

[34] S.-Y. Ahn, W.-J. Jang, J.-O. Shim, B.-H. Jeon, H.-S. Roh, CeO2 -based oxygen storage capacity materials in environmental and energy catalysis for carbon neutrality: extended application and key catalytic properties, Catal. Rev. 66 (2024) 1316–1399, https://doi.org/10.1080/01614940.2022.2162677.

[35] X. Wang, J. Wang, Y. Sun, K. Li, T. Shang, Y. Wan, Recent advances and perspectives of CeO2-based catalysts: electronic properties and applications for energy storage and conversion, Front. Chem. 10 (2022), https://doi.org/10.3389/fchem.2022.1089708.

[36] S. Bagheri, I. Khalil, N.M. Julkapli, Cerium(IV) oxide nanocomposites: catalytic properties and industrial application, J. Rare Earths 39 (2021) 129–139, https://doi.org/10.1016/j.jre.2020.02.022.

[37] D. Primc, B. Belec, D. Makovec, Synthesis of composite nanoparticles using co-precipitation of a magnetic iron-oxide shell onto core nanoparticles, J. Nanoparticle Res. 18 (2016) 64, https://doi.org/10.1007/s11051-016-3374-5.

[38] J. Zhen, X. Wang, D. Liu, S. Song, Z. Wang, Y. Wang, J. Li, F. Wang, H. Zhang, Co3O4@CeO2 core@shell cubes: designed synthesis and optimization of catalytic properties, Chem. Eur J. 20 (2014) 4469–4473, https://doi.org/10.1002/chem.201304109.

[39] C. Cui, M. Tou, M. Li, Z. Luo, L. Xiao, S. Bai, Z. Li, Heterogeneous semiconductor shells sequentially coated on upconversion nanoplates for NIR-light enhanced photocatalysis, Inorg. Chem. 56 (2017) 2328–2336, https://doi.org/10.1021/acs.inorgchem.6b03079.

[40] L. Liu, J. Shi, R. Wang, Facile construction of Mn2O3@CeO2 core@shell cubes with enhanced catalytic activity toward CO oxidation, J. Solid State Chem. 269 (2019) 419–427, https://doi.org/10.1016/j.jssc.2018.10.024.

[41] L. Zhang, J. Pan, Y. Long, J. Li, W. Li, S. Song, Z. Shi, H. Zhang, CeO2 -encapsulated hollow Ag–Au nanocage hybrid nanostructures as high-performance catalysts for Cascade reactions, Small 15 (2019), https://doi.org/10.1002/smll.201903182.

[42] G. Dee, H. Shayoub, H. McNeill, I.S. Lozano, A. Rafferty, Y.K. Gun'ko, MnFe2O4@SiO2@CeO2 core–shell nanostructures for applications in water remediation, RSC Adv. 13 (2023) 10513–10522, https://doi.org/10.1039/D3RA01112G.

[43] S. Gyergyek, D. Makovec, M. Jagodič, M. Drofenik, K. Schenk, O. Jordan, J. Kovač, G. Dražič, H. Hofmann, Hydrothermal growth of iron oxide NPs with a uniform size distribution for magnetically induced hyperthermia: structural, colloidal and magnetic properties, J. Alloys Compd. 694 (2017) 261–271, https://doi.org/10.1016/j.jallcom.2016.09.238.

[44] S. Kralj, D. Makovec, S. Čampelj, M. Drofenik, Producing ultra-thin silica coatings on iron-oxide nanoparticles to improve their surface reactivity, J. Magn. Magn Mater. 322 (2010) 1847–1853, https://doi.org/10.1016/j.jmmm.2009.12.038.

[45] M. Nečemer, P. Kump, J. Ščančar, R. Jaćimović, J. Simčič, P. Pelicon, M. Budnar, Z. Jeran, P. Pongrac, M. Regvar, K. Vogel-Mikuš, Application of X-ray fluorescence

analytical techniques in phytoremediation and plant biology studies, Spectrochim. Acta Part B At. Spectrosc. 63 (2008) 1240–1247, https://doi.org/10.1016/j.sab.2008.07.006.

[46] D. Kumar, I.P.S. Kapoor, G. Singh, U.P. Singh, N. Goel, Lanthanoid metal nitrates with hydrogen bonded hexamethylenetetramine, J. Therm. Anal. Calorim. 114 (2013) 5–18, https://doi.org/10.1007/s10973-012-2826-0.

[47] A. Trzesowska-Kruszynska, R. Kruszynski, M. Zalewicz, T.J. Bartczak, Coordination sphere geometry changes of lanthanoid(III) nitrate complexes with hexamethylenetetramine, J. Coord. Chem. 63 (2010) 1013–1028, https://doi.org/10.1080/00958971003682006.

[48] O.S. Polezhaeva, N.V. Yaroshinskaya, V.K. Ivanov, Formation mechanism of nanocrystalline ceria in aqueous solutions of cerium(III) nitrate and hexamethylenetetramine, Inorg. Mater. 44 (2008) 51–57, https://doi.org/10.1134/S0020168508010081.

[49] P. Abellan, T.H. Moser, I.T. Lucas, J.W. Grate, J.E. Evans, N.D. Browning, The formation of cerium(III) hydroxide nanoparticles by a radiation mediated increase in local pH, RSC Adv. 7 (2017) 3831–3837, https://doi.org/10.1039/C6RA27066B.

[50] Y. Zhang, S. Bals, G. Van Tendeloo, Understanding CeO2 -based nanostructures through advanced electron microscopy in 2D and 3D, Part. Part. Syst. Charact. 36 (2019), https://doi.org/10.1002/ppsc.201800287.

[51] C.B. Whitehead, S. Özkar, R.G. Finke, LaMer's 1950 model of particle formation: a review and critical analysis of its classical nucleation and fluctuation theory basis, of competing models and mechanisms for phase-changes and particle formation, and then of its application to silver halide, s, Mater. Adv. 2 (2021) 186–235, https://doi.org/10.1039/D0MA00439A.

[52] R.C. Baetzold, H. Yang, Computational study on surface structure and crystal morphology of γ-Fe2O3: toward deterministic synthesis of nanocrystals, J. Phys. Chem. B 107 (2003) 14357–14364, https://doi.org/10.1021/jp035785k.

[53] J. Mizele, J.L. Dandurand, J. Schott, Determination of the surface energy of amorphous silica from solubility measurements in micropores, Surf. Sci. 162 (1985) 830–837, https://doi.org/10.1016/0039-6028(85)90986-0.

[54] M. Lin, Z.Y. Fu, H.R. Tan, J.P.Y. Tan, S.C. Ng, E. Teo, Hydrothermal synthesis of CeO2 nanocrystals: ostwald ripening or oriented attachment? Cryst. Growth Des. 12 (2012) 3296–3303, https://doi.org/10.1021/cg300421x.

[55] J. Carrey, B. Mehdaoui, M. Respaud, Simple models for dynamic hysteresis loop calculations of magnetic single-domain nanoparticles: application to magnetic hyperthermia optimization, J. Appl. Phys. 109 (2011), https://doi.org/10.1063/1.3551582.

[56] L.-M. Lacroix, R.B. Malaki, J. Carrey, S. Lachaize, M. Respaud, G.F. Goya, B. Chaudret, Magnetic hyperthermia in single-domain monodisperse FeCo nanoparticles: evidences for Stoner–Wohlfarth behavior and large losses, J. Appl. Phys. 105 (2009), https://doi.org/10.1063/1.3068195.

[57] B. Mehdaoui, A. Meffre, J. Carrey, S. Lachaize, L. Lacroix, M. Gougeon, B. Chaudret, M. Respaud, Optimal size of nanoparticles for magnetic hyperthermia: a combined theoretical and experimental study, Adv. Funct. Mater. 21 (2011) 4573–4581, https://doi.org/10.1002/adfm.201101243.

[58] D. Serantes, D. Baldomir, C. Martinez-Boubeta, K. Simeonidis, M. Angelakeris, E. Natividad, M. Castro, A. Mediano, D.-X. Chen, A. Sanchez, L. Balcells, B. Martínez, Influence of dipolar interactions on hyperthermia properties of ferromagnetic particles, J. Appl. Phys. 108 (2010), https://doi.org/10.1063/1.3488881.

[59] C. Moreau, M.N. Belgacem, A. Gandini, Recent catalytic advances in the chemistry of substituted furans from carbohydrates and in the ensuing polymers, Top. Catal. 27 (2004) 11–30, https://doi.org/10.1023/B:TOCA.0000013537.13540.0e.

[60] F.K. Kazi, A.D. Patel, J.C. Serrano-Ruiz, J.A. Dumesic, R.P. Anex, Techno-economic analysis of dimethylfuran (DMF) and hydroxymethylfurfural (HMF) production from pure fructose in catalytic processes, Chem. Eng. J. 169 (2011) 329–338, https://doi.org/10.1016/j.cej.2011.03.018.

[61] S. Fulignati, C. Antonetti, E. Wilbers, D. Licursi, H.J. Heeres, A.M. Raspolli Galletti, Tunable HMF hydrogenation to furan diols in a flow reactor using Ru/C as catalyst, J. Ind. Eng. Chem. 100 (2021) 390.e1–390.e9, https://doi.org/10.1016/j.jiec.2021.04.057.

[62] S. Liu, Y. Zhu, Y. Liao, H. Wang, Q. Liu, L. Ma, C. Wang, Advances in understanding the humins: formation , prevention and application, Appl. Energy Combust. Sci. 10 (2022) 100062, https://doi.org/10.1016/j.jaecs.2022.100062.

[63] R.-J. van Putten, J.C. van der Waal, E. de Jong, C.B. Rasrendra, H.J. Heeres, J.G. de Vries, Hydroxymethylfurfural, A versatile platform chemical made from renewable resources, Chem. Rev. 113 (2013) 1499–1597, https://doi.org/10.1021/cr300182k.

[64] A. Gandini, Furans in polymer chemistry, Prog. Polym. Sci. 22 (1997) 1203–1379, https://doi.org/10.1016/S0079-6700(97)00004-X.

[65] B. Pomeroy, M. Grilc, S. Gyergyek, B. Likozar, Catalyst structure-based hydroxymethylfurfural (HMF) hydrogenation mechanisms, activity and selectivity over Ni, Chem. Eng. J. 412 (2021) 127553, https://doi.org/10.1016/j.cej.2020.127553.

[66] B. Pomeroy, M. Grilc, B. Likozar, Process condition-based tuneable selective catalysis of hydroxymethylfurfural (HMF) hydrogenation reactions to aromatic, saturated cyclic and linear poly-functional alcohols over Ni–Ce/Al 2 O 3, Green Chem. 23 (2021) 7996–8002, https://doi.org/10.1039/D1GC02086B.

[67] R. Alamillo, M. Tucker, M. Chia, Y. Pagán-Torres, J. Dumesic, The selective hydrogenation of biomass-derived 5-hydroxymethylfurfural using heterogeneous catalysts, Green Chem. 14 (2012) 1413, https://doi.org/10.1039/c2gc35039d.

[68] I. Mustieles Marin, D. De Masi, L.-M. Lacroix, P.-F. Fazzini, P.W.N.M. van Leeuwen, J.M. Asensio, B. Chaudret, Hydrodeoxygenation and hydrogenolysis of biomass-based materials using FeNi catalysts and magnetic induction, Green Chem. 23 (2021) 2025–2036, https://doi.org/10.1039/D0GC03495A.